

Comparison of glancing-angle scatterings on different materials in a high aspect ratio plasma etching process using molecular dynamics simulation

Cite as: J. Vac. Sci. Technol. A **40**, 053007 (2022); <https://doi.org/10.1116/6.0002008>

Submitted: 07 June 2022 • Accepted: 28 July 2022 • Published Online: 01 September 2022

 Yao Du,  Florian Krüger, Sang Ki Nam, et al.



View Online



Export Citation



CrossMark

ARTICLES YOU MAY BE INTERESTED IN

Plasma etching: Yesterday, today, and tomorrow

Journal of Vacuum Science & Technology A **31**, 050825 (2013); <https://doi.org/10.1116/1.4819316>

Plasma etching of high aspect ratio features in SiO₂ using Ar/C₄F₈/O₂ mixtures: A computational investigation

Journal of Vacuum Science & Technology A **37**, 031304 (2019); <https://doi.org/10.1116/1.5090606>

Overview of atomic layer etching in the semiconductor industry

Journal of Vacuum Science & Technology A **33**, 020802 (2015); <https://doi.org/10.1116/1.4913379>



HIDEN ANALYTICAL

Instruments for Advanced Science

■ Knowledge ■ Experience ■ Expertise

Click to view our product catalogue

Contact Hiden Analytical for further details:
W www.HidenAnalytical.com
E info@hiden.co.uk

Gas Analysis

Surface Science

Plasma Diagnostics

Vacuum Analysis

- dynamic measurement of reaction gas streams
- catalysis and thermal analysis
- molecular beam studies
- dissolved species probes
- fermentation, environmental and ecological studies

- UHV TPD
- SIMS
- end point detection in ion beam etch
- elemental imaging - surface mapping

- plasma source characterization
- etch and deposition process reaction kinetic studies
- analysis of neutral and radical species

- partial pressure measurement and control of process gases
- reactive sputter process control
- vacuum diagnostics
- vacuum coating process monitoring

Comparison of glancing-angle scatterings on different materials in a high aspect ratio plasma etching process using molecular dynamics simulation

Cite as: J. Vac. Sci. Technol. A **40**, 053007 (2022); doi: 10.1116/6.0002008

Submitted: 7 June 2022 · Accepted: 28 July 2022 ·

Published Online: 1 September 2022



View Online



Export Citation



CrossMark

Yao Du,^{1,a)} Florian Krüger,² Sang Ki Nam,³ Hoki Lee,³ Suyoung Yoo,³ Jacob Eapen,¹ Mark J. Kushner,² and Steven Shannon^{1,b)}

AFFILIATIONS

¹Department of Nuclear Engineering, North Carolina State University, Raleigh, North Carolina 27695-7909

²Department of Electrical Engineering and Computer Science, University of Michigan, 1301 Beal Ave., Ann Arbor, Michigan 48109-2122

³Mechatronics Research Division, Samsung Electronics Co., Ltd., Suwon 443-742, South Korea

^aElectronic mail: ydu9@ncsu.edu

^bAuthor to whom correspondence should be addressed: scshanno@ncsu.edu

ABSTRACT

In plasma etching for microelectronics fabrication, one of the objectives is to produce a high aspect ratio (HAR) via and trench structures. A principal contributor to the HAR feature shape is the manner in which energetic ions interact with sidewalls inside the feature. The scattering angle and energy loss of ions reflecting from sidewalls determine the sidewall slope and can lead to defects such as microtrenching and bowing. Understanding how ions interact with sidewalls can improve our control of the critical dimensions of HAR features. Ions accelerated in the plasma sheath arrive in the feature with energies as large as a few keV and initially strike the sidewalls at glancing angles. These scattering events extend to the photolithographic mask. Scattering from the mask at glancing angles can produce ions incident into the underlying feature with a broader angular distribution, leading to less desirable feature properties. In this work, results are discussed from Molecular Dynamics (MD) simulations of glancing-angle scattering of argon ions from three materials common to HAR etch: polystyrene (as a photoresist surrogate), amorphous carbon (a hard mask material), and SiO₂ (a common insulating material used in microelectronics devices). Results from simulations reveal a transition from specular scattering to diffuse scattering as the angle of the incident ion decreases (90° being glancing incidence) and incident energy increases. Scattering from polystyrene is more diffuse compared to amorphous carbon and SiO₂ for identical incident ion conditions.

Published under an exclusive license by the AVS. <https://doi.org/10.1116/6.0002008>

I. INTRODUCTION

As characteristic dimensions of integrated circuits approach single atomic layers, improving device performance now depends on combining device scale length reduction, new materials, and new device geometries, including stacking of planar devices¹ (i.e., three-dimensional structures). This is particularly the case in fabrication of high-density memory in which up to 512 alternating layers of, for example, SiO₂ and Si₃N₄ form the material basis of

the device.² Fabrication requires plasma etching of high aspect ratio (HAR) vias through this stack. Aspect ratio (AR) is the ratio of the height to the width of the feature. A via is a vertical, cylindrical hole. The AR of such vias can exceed 100:1 in 3D-NAND memory devices.^{3,4}

The fabrication of HAR vias and trenches is typically performed using plasma etching in capacitively coupled plasmas.^{5,6} Acceleration of ions in the plasma sheath at the surface of the

wafer produces an anisotropic angular distribution of ions incident onto the wafer (angular spread less than a few degrees) with energies as large as a few keV. The narrow angular distribution is intended to enable energetic ions to exclusively strike the bottom of the feature.^{7,8} However, for any finite angular spread, there will be an AR for which ions collide with the interior sidewalls of the feature, typically at glancing angles. (Here, a 90° angle of incidence is glancing to the surface; a 0° angle of incidence is normal to the surface.) Smaller angles of incidence may result from charging of surfaces inside the feature, producing lateral electric fields that deflect ions whose subsequent collisions with surfaces distort the feature's cross section profile. Near specular glancing angle scattering may produce microtrenching as ion energy is focused near the sidewalls at the bottom of the feature.^{9,10} (In this discussion, an ion refers to both the incident particle and the hot neutral particle after an ion neutralizes upon striking a surface.) With multiple sidewall scattering events, ion energy may be reduced to the point that etching cannot be activated, thereby terminating the etch process at some critical depth.^{11–13} Understanding how ions interact with the sidewalls of HAR features at the glancing angle is important to optimize plasma etching processes.

Molecular dynamics (MD) simulations have been extensively used for investigating how ions interact with materials across a broad spectrum of applications, spanning radiation damage in nuclear materials,¹⁴ radiation interaction with biological systems,¹⁵ and plasma-assisted processes¹⁶ such as etching of conductors and dielectrics. MD simulations have been used to investigate Ar⁺ and Cl⁺ processes for etching silicon,¹⁷ reactive ion etching of Si and SiO₂ by fluorine-rich ion species^{18,19} and SF₅⁺ ions,²⁰ near-surface modification of polystyrene by argon ions,²¹ and the surface reaction kinetics of etch-by-product for SiCl_x⁺ ions incident on Si(100) surfaces.²² The emphasis has been on how energetic ions erode or modify the material being processed as well as the synergistic interaction of the ions, reactive species, and plasma facing surfaces.

Optimizing the fabrication of HAR vias and trenches requires an understanding of how ions propagate through these HAR features. Ion bombardment of the mask material causes mask erosion. Consecutive scattering events with the sidewalls can modify both the trajectory and energy of the ion as it moves deeper into the HAR feature. The selectivity between etching the underlying material and the mask defining the feature is finite (typically from 5 to 20). As a result, mask materials may themselves have AR of 5–20 in order that they do not erode prior to finishing etching an AR = 100 feature in the underlying materials. The AR of the mask is large enough that ion scattering may occur from the sidewalls of the mask before the ions reach the underlying materials. These sequential sidewall scatterings from both the mask and from the feature material will broaden the angular distribution and lower the ion energy. Of particular interest is the evolution of ion trajectories and energies from the mask where erosion may produce sloping sidewall angles and/or the mask intentionally has a sidewall slope.

Profile simulators (models that predict the evolution of features given the incident reactive fluxes from the plasma) address scattering from sidewalls inside features with varying degrees of sophistication, accounting for specular and diffusive scattering, and energy loss. A better understanding of these scattering processes, incorporated into profile simulations, will improve predictions of

the energy and angle distributions of ions as they traverse HAR features. Profile simulations will then have improved capability to predict fabrication of HAR features and so guide process development. In the results discussed in this paper, molecular dynamic simulations were employed to study these glancing angle scattering processes to improve this predictive capability and guide the evolution of HAR process conditions for increasingly challenging aspect ratio features.

A typical HAR feature consists of a mask layer and an etch layer. The mask layer may consist of a top layer of photoresist (PR), typically a radiation-sensitive hydrocarbon polymer that is used to establish patterns in optical or beam-driven lithographic processes²³ (see Fig. 1). The PR may sit on top of a dielectric intended to mitigate light reflection during optical lithography patterning of the polymer layer (an anti-reflection coating) or on top of a more etch-resistant "hard mask" that provides additional definition to the etch layer during pattern formation.²⁴ The etch layer is the material in which the feature is being fabricated, generally classified as dielectric (e.g., SiO₂ and Si₃N₄) and/or conductor (e.g., Si and Ge).²⁵ In 3D devices, such as NAND memory, the etch layer can consist of layers of different materials such as silicon dioxide and silicon nitride that are used to eventually form vertical stacks of memory cells.²⁶

Materials used in MD simulations are typically either the actual material or a surrogate material that has well-understood atomic scale properties while being representative of the composition and properties of the actual material. For example, previous

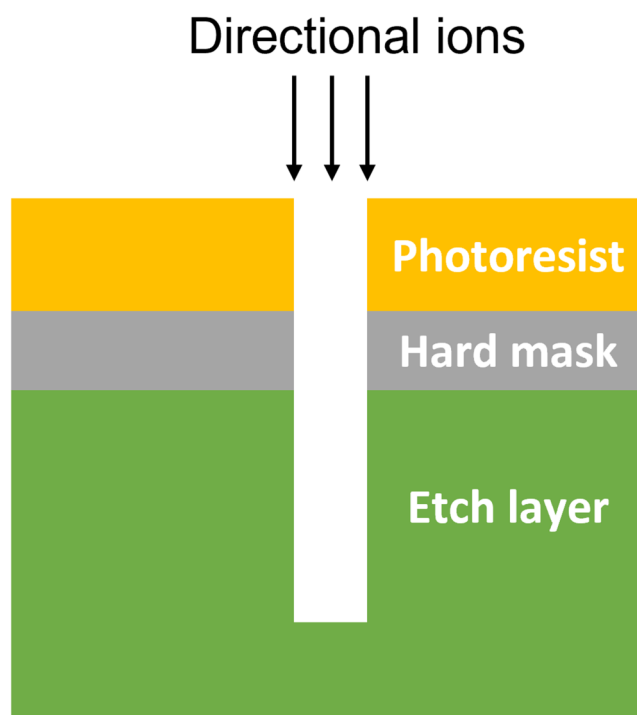


FIG. 1. Cross section view of a typical HAR feature with a multilayer structure.

modeling efforts^{16,21,27} used polystyrene (PS) as a representative material of 248-nm photoresist for its simpler chemical composition and for being well studied in MD community. Amorphous carbon (AC) is a common hard mask material in microelectronics manufacturing processes while also having reliable mechanical, chemical, and electronic properties.^{28,29} Dielectrics in plasma etching often contains silicon compounds⁶ such as SiO_2 and Si_3N_4 both of which have well-validated atomic scale models for molecular dynamic simulations.³⁰

In this paper, we discuss results from MD simulations of glancing-angle scattering of ions from materials of interest to HAR plasma etching processes. Specifically, PS (as a surrogate for photoresist), AC (as a hard mask candidate), and SiO_2 (as a dielectric etch layer) were investigated. Validation of computationally synthesized material structures for the simulations was performed by comparing structural and thermodynamic properties of the materials with previous computational and experimental studies with there being overall good agreement. Results of the simulations showed a transition from nearly elastic specular scattering to inelastic diffuse scattering as the incident angle of the ions became more normal to the surface and as the incident energy of the ion increased. Overall, more diffuse scattering occurred for scattering from PS surfaces compared to AC and SiO_2 . The MD simulations were performed using the Large-scale Atomic/Molecular Massively Parallel Simulator³¹ (LAMMPS). The computational methods and procedures are discussed in Sec. II. Validation and results for ion scattering results are discussed in Secs. III and IV. Conclusions are summarized in Sec. V.

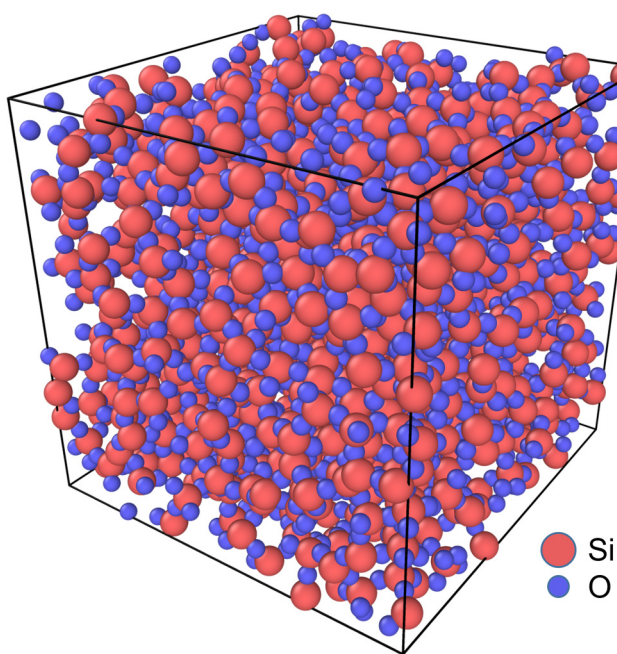


FIG. 2. Equilibrated state of amorphous SiO_2 at 300 K and the final size of the simulation box is $(35.18 \text{ \AA})^3$, corresponding to a density of 2.288 g/cm^3 .

II. COMPUTATIONAL METHODS

In performing MD simulations, the material to be investigated must be prepared. This means that computational atoms composing the material (e.g., Si and O atoms for SiO_2) must be arranged in a manner that produces the desired stoichiometry and topology (e.g., crystalline vs amorphous, defect free or with defects). In this section, the methods and procedures for computationally preparing the materials and performing ions scattering simulations are discussed.

A. Materials preparation

Amorphous SiO_2 was prepared using a quenching procedure.³² A system of 1000 Si atoms and 2000 O atoms were randomly distributed in a $(35.1 \text{ \AA})^3$ cubic box corresponding to a density of 2.307 g/cm^3 . Before quenching, the system was heated to 5000 K using an NPT (isothermal-isobaric) ensemble at 0 pressure for a total of 300 ps using the Nose-Hoover thermostat and the barostat.³³⁻³⁵ The NPT ensemble is a concept in statistical mechanics that describes a system where the number of particles (N), the pressure (P), and the temperature (T) of the system are kept constant. The temperature and pressure of the simulation cell are

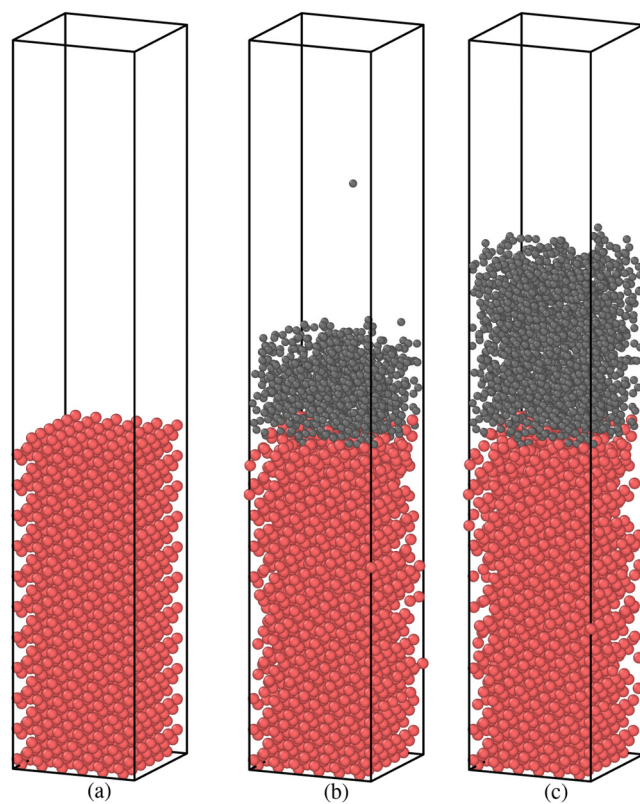


FIG. 3. Examples of C atoms deposited on a Si substrate: (a) initial Si substrate, (b) 1000 C deposited, and (c) 2000 C deposited. The computational domain is $23 \times 23 \times 120 \text{ \AA}^3$.

constrained by adjusting particle velocities and domain dimensions, respectively. After the system was thermodynamically equilibrated, it was quenched to 300 K with a cooling rate of 1 K/ps. The system was then relaxed in an NPT ensemble to enable the system to freely expand or shrink, reducing both the internal stresses and energies. The final state of amorphous SiO₂, when the thermodynamic parameters have reached a steady state condition, is shown in Fig. 2. The simulations were performed with periodic boundary conditions using an integration time step of 1 fs. For SiO₂, we used the interatomic potential developed by Munetoh *et al.*,³² which is a Tersoff potential³⁶ parameterized specifically for the Si-O system.

For AC, the simulation cell was prepared following the procedure used in a previous work³⁷ by growing an AC layer. The AC growth was simulated with a carbon deposition procedure on a 23 × 23 × 59.7 Å³ silicon(100) crystal substrate. With a lattice constant of 5.4307 Å, a Si substrate structure was first simulated using 1584 Si atoms. The substrate was equilibrated at 300 K in an NVT [canonical, same as the NPT ensemble except volume (V) is kept constant instead of pressure (P)] ensemble for 30 ps. Following equilibration, 2000 carbon atoms were deposited randomly and sequentially on the top of the silicon substrate surface. C atoms were directed onto the surface at normal incidence with an energy of 1 eV. During deposition, the substrate was maintained at 300 K using a time step of 0.5 fs in an NVT ensemble. The time interval between launching C atoms was 2 ps to allow the substrate to fully relax after the previous atom interacted with the substrate. The sequential deposition of C atoms is shown in Fig. 3. To simulate a semi-infinite large substrate, periodic boundary conditions were enforced along lateral directions while the bottom two layers of silicon atoms were fixed. The interatomic potential used in this Si-C system was developed by Erhart and Able,³⁸ which is a Tersoff potential³⁶ parameterized specifically for silicon, carbon, and silicon carbide system.

PS is somewhat more complex to model. The Transferable Potentials for Phase Equilibria-United Atom (TraPPE) force field³⁹ was used to describe this hydrocarbon polymer. The values of

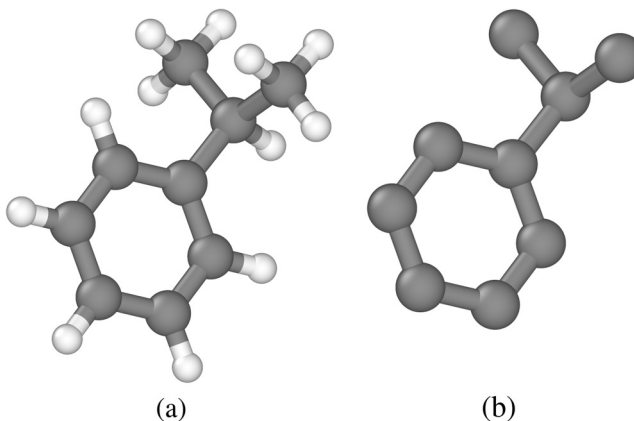


FIG. 4. Monomer of PS shown in (a) a typical model with both C and H atoms and (b) a united atom model.

parameters in the TraPPE force field used in this work were taken from Refs. 40 and 41. Due to limitations in LAMMPS, a harmonic bond potential⁴² was used in the place of fixed-length bonds as used in the original work.³⁹ With TraPPE force fields, bonds, angles, and dihedrals interactions are explicitly defined. The carbon atoms are connected to the neighboring hydrogen atoms to form macroatoms as shown in Fig. 4. The system was constructed with 10 chains of PS with each chain containing 40 monomers so that the molecular weight of the polymer chain is consistent with commercial photoresists and published results.^{21,40,41,43}

The chains were randomly placed and oriented in a box with periodic boundary conditions.⁴⁴ Several postprocessing steps were needed to properly define the united-atom model and topology required by the TraPPE force field. The initial size of the simulation box was (51.7 Å)³ (51.7 Å on a side), which corresponds to a density of ~0.5 g/cm³. The system was then heated to 600 K using an NPT ensemble at atmosphere pressure, maintaining temperature and pressure for 4 ns using a timestep of 2 fs. After equilibration, the system was steadily cooled to 300 K and further equilibrated for 2 ns. The final system was stable and denser than prior to equilibration with a density closely matching typical PS (~1.0 g/cm³). The final state of the polymer system is shown in Fig. 5.

B. Ions scattering

After producing the three etching-layer structures for SiO₂, PS, and AC, ion scattering was simulated from the top surface of each material, as shown schematically in Fig. 6. Ions with energy E_{in} were incident on the surface of the MD generated structure at

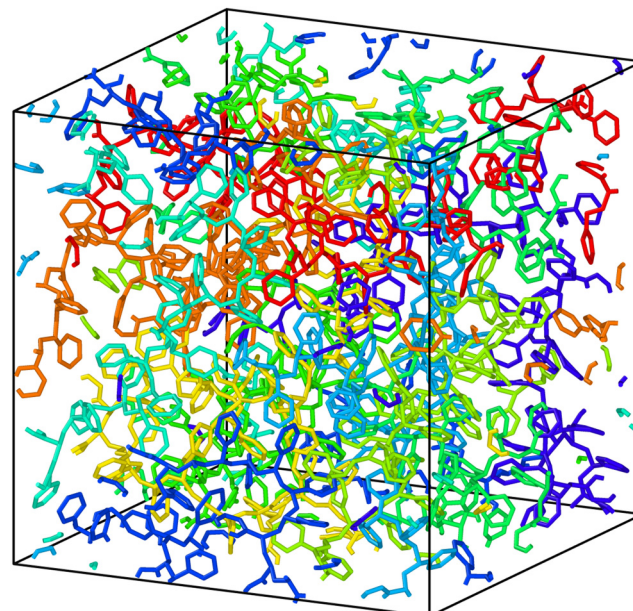


FIG. 5. Equilibrated state of the simulated PS system at 300 K, with 10 chains each containing 40 monomers. The chains are colored separately.

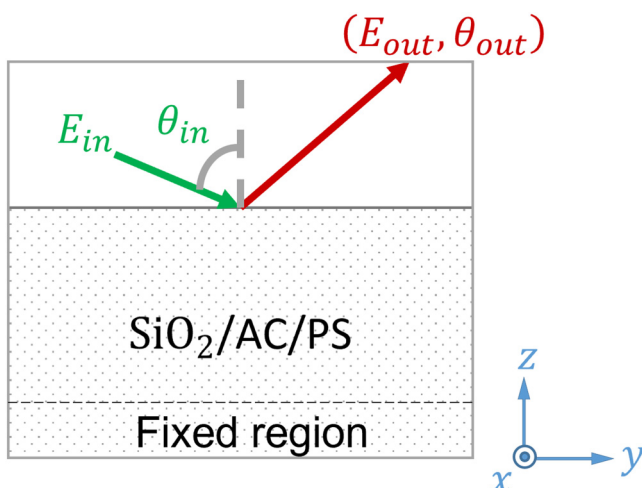
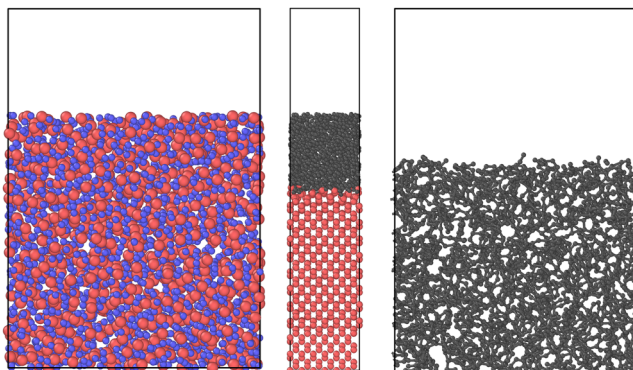


FIG. 6. Schematic showing the ion scattering geometry.

an angle of incidence θ_{in} defined as the angle between the surface normal and incident ion velocity vector. The exit energy E_{out} and exit angle θ_{out} for the scattered ions were recorded. Some modifications to the computational domain were also made to facilitate these scattering simulations. The boundary condition in the z (vertical) direction was changed from periodic to finite to allow reflected ions to leave the simulation domain. The boundary conditions in the x and y directions (horizontal) were kept periodic. A thin layer was removed from the top of the material to smooth the surface. The atomic positions in the bottom layers of the simulation cell ($\sim 20\%$ of the total volume) were fixed to simulate a semi-infinite large substrate. A final equilibration step was then performed to ensure that the simulation cell was stable. The equilibrated structures used for ion scattering are shown in Fig. 7.

This study focuses primarily on physical ion interactions more so than reactive surface modifications that would be more impacted

FIG. 7. Front view of simulation cells prior to ion scattering: (left) SiO₂ with width 35.18 Å, (middle) AC with width 23 Å, and (right) PS with width 40.27 Å.

by ion selection, particularly a reactive species such as chlorine. Thus, singly ionized argon ions were used to investigate glancing-angle scattering. The Ziegler-Biersack-Littmark (ZBL) screened nuclear repulsion potential⁴⁵ was used to describe the interaction between the argon ions and the target atoms (Ar-Si, Ar-O, and Ar-C). The ZBL potential has been widely used in ion-induced modification of materials and is commonly combined with other interatomic potentials such as EAM, SW, and Tersoff.^{46-48,59} The ZBL potential between two particles i and j is given by

$$E_{ij}^{ZBL} = \frac{1}{4\pi\epsilon_0} \frac{Z_i Z_j e^2}{r_{ij}} \phi(r_{ij}/a) + S(r_{ij}), \quad (1)$$

where ϵ_0 is the permittivity of vacuum, Z_i and Z_j are the atomic numbers, e is the elementary charge, r_{ij} is the interatomic distance, ϕ is a screening parameter defined by a scale length a , and $S(r_{ij})$ is a switching function for smoothly transitioning the whole function to 0 after the cutoff distance. For PS, the total atomic number of each macroatom is used in the ZBL potential. It can be seen from Eq. (1) that no electronic charge term was included in the ZBL potential, so ions and neutrals will be treated the same from an interatomic force standpoint. This can be justified by assuming that the incident ion will neutralize by Auger recombination prior to actually striking the surface. This assumption is consistent with published MD works^{18,49} in plasma etching.

Ions are introduced at random (x, y) positions along a plane parallel to the surface at a distance that exceeds the cutoff of the ZBL potential. 2000 Ar ions are directed toward the surface for each incident energy E_{in} and angle θ_{in} . The target material was allowed to equilibrate between collisions. To minimize the effect of cumulative damage to the surface, the target configuration was reset to its initial state after every 10 collisions. In a typical plasma etching process, the surface conditions will be affected by several surface processes such as chemical etch, polymer deposition, roughening, striations, mask reticulation, etc. In this work, we chose to focus on pristine surfaces to generate ions scattering data relatively independently. The results from this work could be further incorporated in the future into profile simulators where the surface damage effect has been included. The energy and angle of each scattered ion (E_{out} and θ_{out}) were recorded after the scattered ion leaves the simulation domain.

The parametric study consisted of θ_{in} ranging from 65° to 89° (every 2°) and E_{in} ranging from 10 to 5000 eV using 10 energies evenly spread on a log scale for E_{in} . The results from each individual (E_{in}, θ_{in}) were then used to construct a two-dimensional distribution of (E_{out}, θ_{out}).

III. VALIDATION OF THE MATERIAL PROPERTIES

In this section, the methods for validating the prepared target materials are discussed. The structural and thermodynamic properties were validated with those from previous studies and comparison to published experimental data. Overall, the current results show good agreement with the published data.

The structures for SiO₂, AC, and PS were validated using the radial distribution function (RDF). For SiO₂, the amorphous structure was benchmarked against previous simulation data³² using

classical MD, as well as with experiment data⁵⁰ obtained from neutron scattering, as shown in Fig. 8. The location of the first two major peaks in the RDF, corresponding to the Si-O and O-O separation distances, respectively, in a [SiO₄] tetrahedral structure, match the two reference results. The second peak in the simulations shows a split, which is a signature of a disordered structure. The location of the third and fourth peaks also agree with nearly the same magnitude. The partial RDFs (not shown) also have good agreement with the reference results.³² The density calculated from the simulations is 2.288 g/cm³, which is close to the experimental value of 2.203 g/cm³. Overall, the interatomic potential used in the simulation is able to predict the amorphous state of silica well.

Similarly, the RDF was used for validating the properties of AC. As shown in Fig. 9, the RDF of the simulated structure agrees well with that from previous *ab initio* MD results⁵¹ as well as with experiment data from electron microscopy. Both the peak locations and the overall shape of the RDF are in reasonable agreement with the reference results. The first and second peaks are sharper in simulations while they are more diffuse in the experiments. The simulated results are in better agreement with the *ab initio* MD data. Note that the simulated density of 2.25 g/cm³ is larger than the experimental value of 1.55 g/cm³. It is known that carbon atoms can form numerous atomic structures with densities ranging from below 1 g/cm³ to above 3 g/cm³. Previous research⁵² showed that although the density of AC does not affect the shape of the RDF significantly, the locations of the RDF peaks shift slightly to the right with increasing density.

In addition to the RDF, the fraction of carbon atoms with *sp*³ hybridization was also evaluated for validation. The *sp*³ fraction is generally positively correlated to the density of the system. In one study,⁵² it was reported that a density of 2.0 g/cm³ corresponds to a *sp*³ fraction of 6.4% while a density of 2.6 g/cm³ corresponds to 43.2%. The estimated *sp*³ fraction of 13.3% with a density of 2.25 g/cm³ obtained from the current work is consistent with these

previous estimates. In another study,⁵¹ a lower density (below 1.6 g/cm³) was shown to correspond to less than 10% *sp*³ fraction. This estimate is also in agreement with the data obtained in this work.

For PS, additional validation was performed due to the more complex structure of the polymer. A parametric study of temperature, ranging from 300 to 800 K with a step of 50 K, was conducted using an NPT ensemble, and the density, dimensions, and diffusion constant of the system were calculated. The density of the PS and the length of the periodic simulation box are plotted as a function of temperature in Fig. 10(a). A typical experimental value for the density of PS is 1.05 g/cm³ at room temperature, and results from simulations agree with this value. The computed linear thermal expansion coefficient is

$$\alpha_L = \frac{1}{L} \frac{dL}{dT}, \quad (2)$$

where *L* is the length of the simulation box and *T* is the temperature. Results from the model produce $\alpha_L = 270 \times 10^{-6}$ K⁻¹ while typical experimental measurements⁵⁴ have a range of $(30-210) \times 10^{-6}$ K⁻¹, indicating that the simulated PS is softer. The diffusion constant is plotted as a function of reciprocal temperature on a semilog plot in Fig. 10(b), which is intended to show an Arrhenius relationship. An Arrhenius relationship describes the temperature dependence of a transport coefficient or a rate constant, *k*, in terms of an activation energy, *E_a*, as follows:

$$k = A \exp\left(-\frac{E_a}{RT}\right), \quad (3)$$

where *R* is the universal gas constant, *T* is the temperature, and *A* is a constant. The derived diffusion coefficient shown in Fig. 10(b) indicates single activation energy (straight line) and diffusion is a

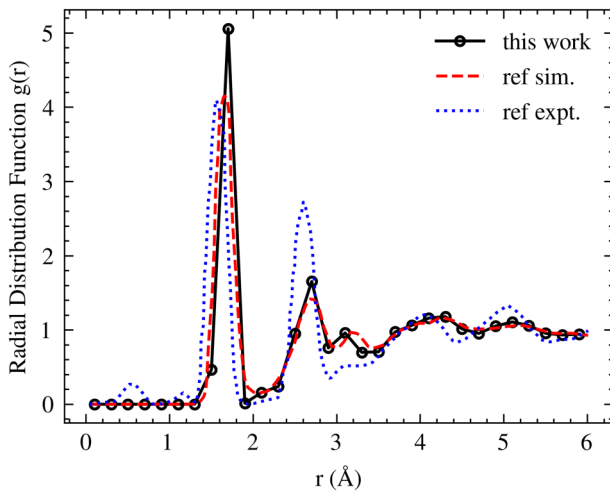


FIG. 8. Radial distribution function $g(r)$ for SiO₂ glass (this work, simulation results from Ref. 32 and experimental data from Ref. 50).

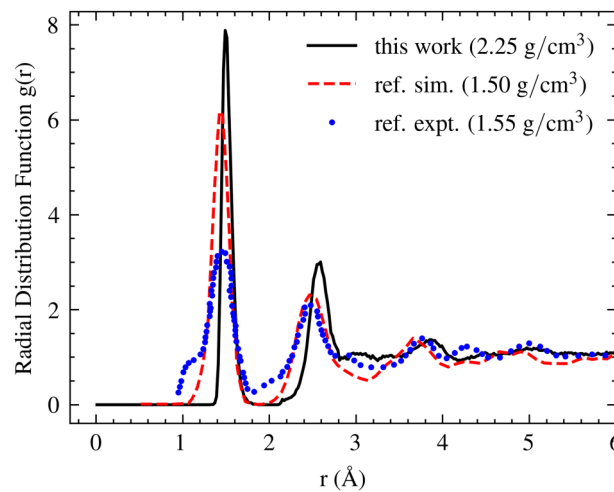


FIG. 9. Radial distribution function $g(r)$ for AC (this work, simulation results from Ref. 51 and experimental data from Ref. 53).

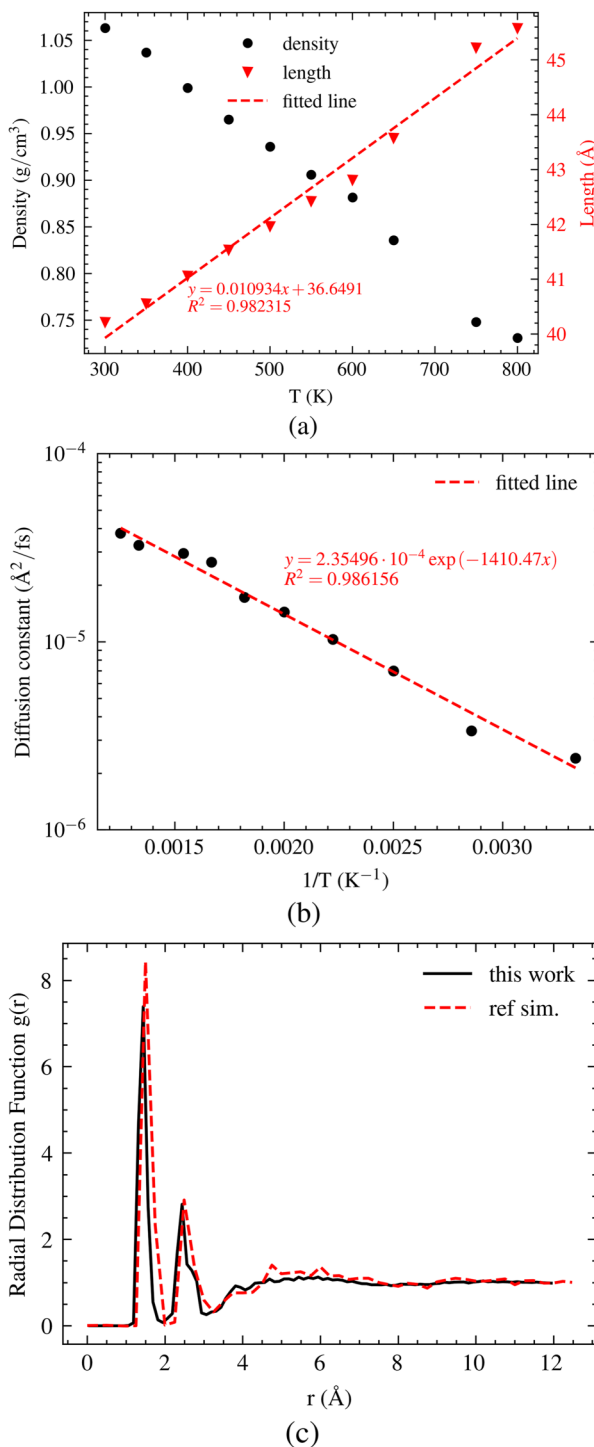


FIG. 10. Structural and thermodynamic studies of PS: (a) density and length (of simulation box) as a function of temperature; (b) diffusion constant as a function of temperature reciprocal in a semilog plot; and (c) radial distribution function $g(r)$ (this work and simulation results from Ref. 40).

simple linear process. The simulated RDF for PS is compared with previous MD simulation results⁴⁰ using the same TraPPE united-atom model in Fig. 10(c). Both the overall shape and the positions of the peaks obtained from these simulations match previous results.

Cell size tests were also performed for all the MD systems described in this work. The total number of atoms for SiO_2 was varied from 3000 to 10 000 while keeping the same Si:O ratio. For AC, the horizontal dimension of the crystalline silicon and the number of deposited carbon atoms were scaled up with the same ratio (from 1.0 to 2.0). The number of chains for PS was also varied from 10 to 20. The size of the simulation box was adjusted accordingly. The results show that the RDFs are invariant with respect to system sizes over the range investigated, indicating that the chosen system sizes (described in Sec. II) for all the three materials were adequate for generating accurate MD results.

IV. ANGULAR DISTRIBUTION OF ION SCATTERING

In this section, results from the simulations for glancing-angle scattering of argon ions from PS, AC, and SiO_2 are discussed. A parametric study of incident angle θ_{in} (75° – 89°) and incident energy E_{in} (10–5000 eV) was conducted. The after scattering probability distribution $f_{E_{\text{in}}, \theta_{\text{in}}}(E_{\text{out}}, \theta_{\text{out}})$ for angle θ_{out} and energy E_{out} were collected on a grid of 20×20 equal-size bins in a range of $[0, 90^\circ] \times [0, E_{\text{in}}]$. $f_{E_{\text{in}}, \theta_{\text{in}}}(E_{\text{out}}, \theta_{\text{out}})$ was normalized so that the probability distributions integrate to unity. These $f_{E_{\text{in}}, \theta_{\text{in}}}(E_{\text{out}}, \theta_{\text{out}})$ are shown in Fig. 11 for a constant incident energy $E_{\text{in}} = 316$ eV at $\theta_{\text{in}} = 75^\circ, 79^\circ, 85^\circ$, and 89° (left to right) for SiO_2 , AC, and PS (top to bottom). Results are also shown for constant incident angle $\theta_{\text{in}} = 79^\circ$ at $E_{\text{in}} = 20, 79, 316$, and 1257 eV (left to right) for SiO_2 , AC, and PS (top to bottom).

The distributions $f_{E_{\text{in}}, \theta_{\text{in}}}(E_{\text{out}}, \theta_{\text{out}})$ generally peak at the position of $(E_{\text{in}}, \theta_{\text{in}})$ and extend to the lower right half of the domain, which shows a transition from specular, elastic reflection to diffuse reflection with a commensurate loss in energy. The scattering is more specular for larger values of θ_{in} and lower values of E_{in} and more diffusive otherwise. A low-energy tail in after scattering distribution occurs in highly diffusive cases, especially for PS. This is because in such cases the close-to-normal scattering with high incident energy results in large fraction of ions penetrating the material and then exiting the material after many collisions and scattering events, resulting in substantial energy loss compared to E_{in} .

The distributions $f_{E_{\text{in}}, \theta_{\text{in}}}(E_{\text{out}}, \theta_{\text{out}})$ shown in Fig. 11 can be summarized by their first and second moments as a function of incident ion parameters. The fractional retained energy of the scattered ions as a function of E_{in} and θ_{in} is shown in Fig. 12. The solid lines are the 50% quantile (median) of normalized E_{out} with the shaded areas extending from the 25% quantile to the 75% quantile. The incident energy is mostly retained for ions having larger values of θ_{in} and lower values of E_{in} . For example, for $\theta_{\text{in}} = 89^\circ$, the incident energy was nearly 100% retained for all materials across the incident energy range. For incident ions at $\theta_{\text{in}} = 75^\circ$ and $E_{\text{in}} > 1000$ eV, more than 50% of the ions lost at least half of their incident energy regardless of the material. In some generally more diffuse cases, the fractional retained energies seem to have minimum values as a function of E_{in} . One possible

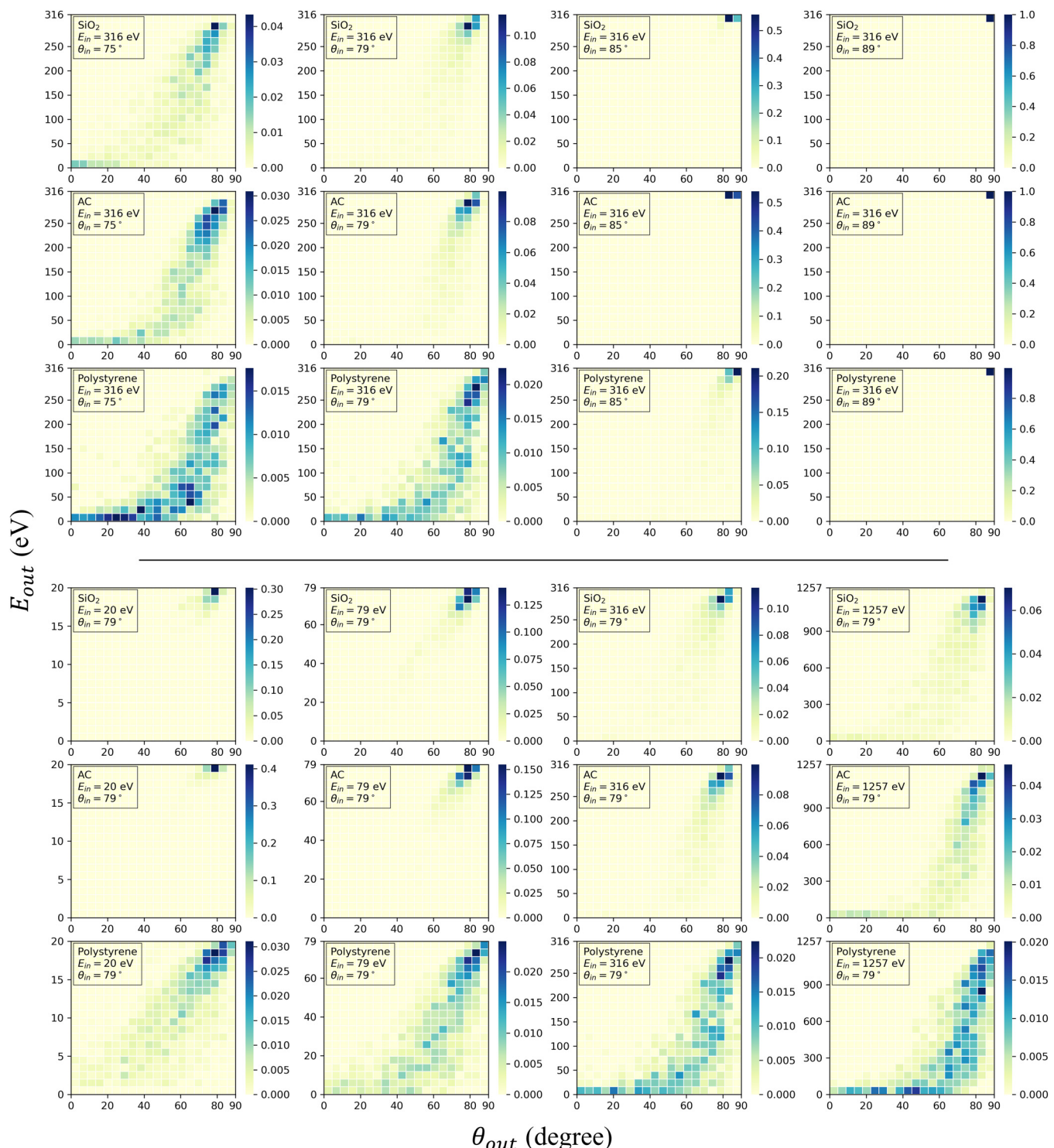


FIG. 11. Comparison of $f_{E_{in}, \theta_{in}}(E_{out}, \theta_{out})$ for different materials, incident energies and incident angles (xaxis $\rightarrow \theta_{out}$, yaxis $\rightarrow E_{out}$, colorscale \rightarrow magnitude), presented in the matrix form: (**Upper matrix**) Constant incident energy $E_{in} = 316 \text{ eV}$ at $\theta_{in} = 75^\circ, 79^\circ, 85^\circ, \text{ and } 89^\circ$ (left to right) for SiO_2 , AC , and PS (top to bottom); (**Lower matrix**) Constant incident angle $\theta_{in} = 79^\circ$ at $E_{in} = 20, 79, 316, \text{ and } 1257 \text{ eV}$ (left to right) for SiO_2 , AC , and PS (top to bottom).

explanation is that it is expected to see more surface damage in such cases even after a few ion incidences, which could affect scattering distributions. Another possible reason is that the span of the incident energy for the last few data points is much wider and the

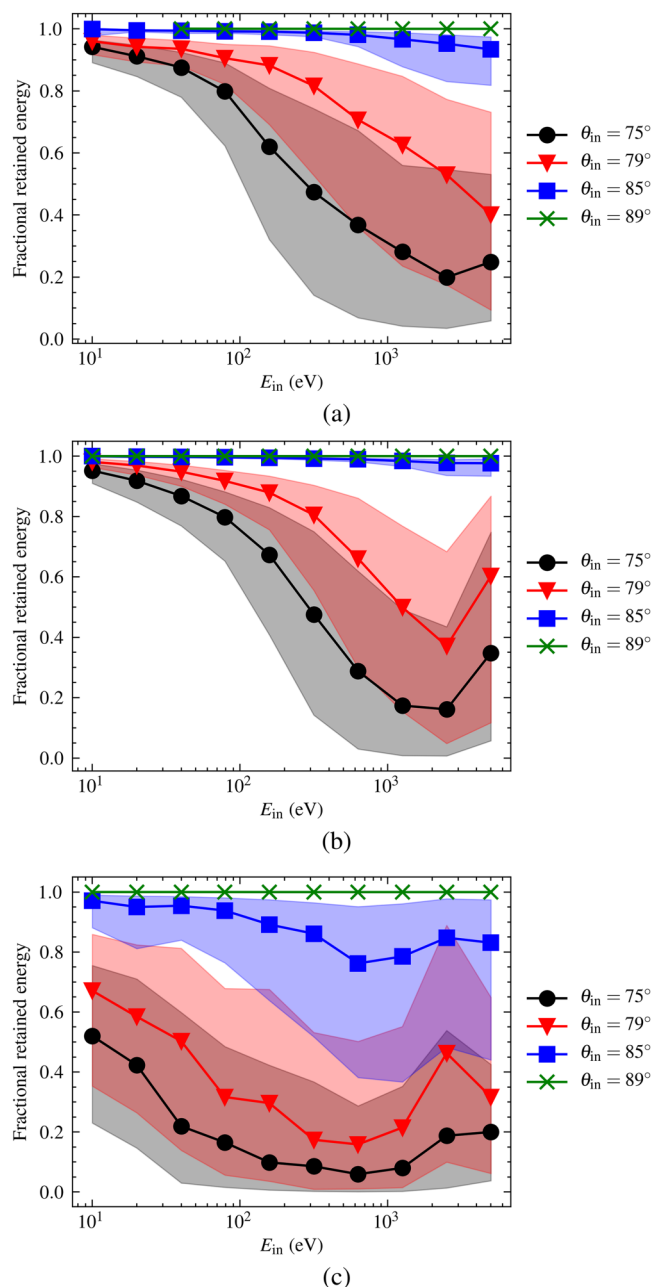


FIG. 12. Fractional retained energy vs E_{in} for SiO_2 , AC, and PS (top to bottom). The data presented are quantiles of E_{out} normalized by E_{in} : solid line is median (50% quantile) and shaded area (colored correspondingly) is from 25% quantile to 75% quantile.

number of collected reflected ions is much smaller in such cases, which could lead to overall significant statistical errors.

There is material dependence on scattering distributions, particularly for PS compared to AC and SiO_2 . The scattering distributions $f_{E_{\text{in}}, \theta_{\text{in}}}(E_{\text{out}}, \theta_{\text{out}})$ are more diffuse for PS compared to either SiO_2 or AC. This can be explained by estimating the total interatomic force an incident ion will experience as well as the structural uniformity for different materials. The ZBL potential was used to describe the interatomic forces between Ar ions and the target atoms. The ZBL potential differentiates atoms only by their atomic numbers [see Eq. (1)]. SiO_2 and AC have similar amorphous structure, and the number density of SiO_2 (0.0689 \AA^{-3}) is 50% lower than AC (0.1133 \AA^{-3}), while the atomic numbers of Si(14) and O (8) atoms are higher than for C(6) atoms. Thus, it is expected to see the same level of interatomic forces being experienced by the ions when interacting with those two materials, therefore giving similar scattering results. The structure of PS contains multiple molecular chains, producing a structure less uniform and more anisotropic compared to the amorphous structure for SiO_2 and AC. This nonuniformity affects the surface roughness at an atomic level and makes the scatterings significantly more diffuse.

The rate of reflection was also investigated as a function of E_{in} and θ_{in} , with the results shown in Fig. 13. The rate of reflection was estimated by the total number of ions leaving the simulation box through the top boundary. The remaining ions were either embedded into the material or the ions slowed due such a degree that they did not leave the simulation domain within the simulation time ($\sim 5 \text{ ps}$ for the last incident ion). These slow ions typically have energies below the thresholds for etching. The rate of reflection follows the transition from specular, elastic reflection to diffuse reflection. Those ions with larger values of θ_{in} (more parallel to the surface) and lower values of E_{in} are more likely to be reflected. This suggests that for an ion interacting with a surface at these glancing angles, the transition from specular to diffuse reflection is related to the number of target atoms the ion collides with. For ions with higher incident energy and lower incident angle, the depth into the material that the ion can penetrate is larger and the number of target atoms the ion can interact with increases. These interactions are cumulative resulting in greater energy loss and deviation from the angle of incidence. For the same incident ($E_{\text{in}}, \theta_{\text{in}}$), more ions are embedded into PS than SiO_2 and AC, which is consistent with PS (1.05 g/cm^3) having a lower mass density than SiO_2 (2.288 g/cm^3) and AC (2.25 g/cm^3).

These results were compared with published data^{17,55} by Graves *et al.* They have performed MD simulations of Ar^+ and Cl^+ impacting onto Si and SiO_2 surfaces, with incident energies below 200 eV and with a wide range of incident angle. Apart from the incident energy, there are differences between their work and our simulations. First, their SiO_2 was initially crystalline, with ion bombardment being used to increase roughness. In this work, we used amorphous SiO_2 with the top surface being smoothed prior to ion scattering. Second, Graves *et al.* simulated scattering of 300–800 ions while retaining the material damage during the scattering process. In this work, the material was restored to its initial smooth state after every 10 incidence ions, which was intended to reduce the effect of material damage induced by high energy ions. Therefore, it is expected to see more specular scattering for the

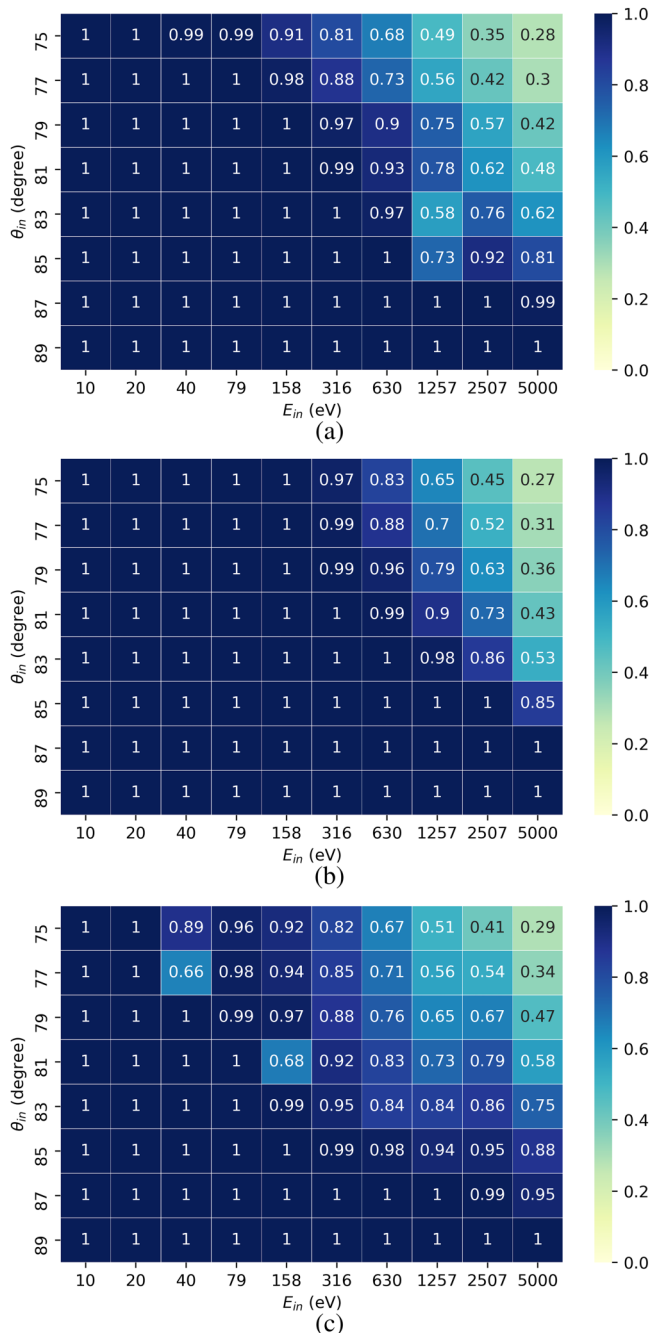


FIG. 13. Rate of reflection (color scale, also numbered in each bin) as a function of E_{in} (x axis) and θ_{in} (y axis) for SiO_2 , AC, and PS (top to bottom).

same incident conditions in this work than in the results of Graves *et al.* Qualitatively, the shape of the distribution $f_{E_{in},\theta_{in}}(E_{out}, \theta_{out})$ for θ_{in} of 75° and 85° with E_{in} below 200 eV and the transition from diffuse to specular scattering when increasing θ_{in} are

consistent with Graves *et al.* The reflection rates in their work for θ_{in} of 75° and 85° and E_{in} of 100 eV are about 0.8 and 1.0, respectively, which are slightly lower than the rate in this work as expected. A low energy tail was also observed in their work for normal incidence. In this work, the low energy tail appeared for high incident energies while the mechanism behind is the same.

V. CONCLUSIONS

In this work, we have performed MD simulations of glancing-angle scattering on different sidewall materials typically exposed to energetic ions during HAR processes, including SiO_2 , AC, and PS. The results of this study indicate a transition from predominantly specular scattering to more diffusive scattering as the incident ion angle becomes more normal and as the incident ion energy increases. This transition to diffusive scattering is accompanied by increased ion energy loss and a higher likelihood of implanting into the material or a near-total ion energy loss. The angles over which this transition occurs are very relevant for typical HAR processes, particularly when the faceting of the mask due to ion erosion is considered. These trends in scattering are consistent with current practice in HAR processing in which greater incident ion energies are used to achieve higher aspect ratios. These trends also suggest that ion energy loss could contribute to RIE (reactive ion etching) lag and etch stop at higher aspect ratios where a large number of sidewall collisions are expected as the ion traverses from the top to the bottom of an HAR feature.

ACKNOWLEDGMENTS

This work was supported through a grant from Samsung Electronics, Mechatronics Research and Development Division. Most of the MD simulations were performed using the high-performance computing resources provided by North Carolina State University. The author would also like to acknowledge the help of several open-source softwares^{56–58} that were used for data visualization and postprocessing.

AUTHOR DECLARATIONS

Conflict of Interest

The authors have no conflicts to disclose.

Author Contributions

Yao Du: Conceptualization (equal); Data curation (equal); Formal analysis (equal); Investigation (equal); Methodology (equal); Resources (equal); Software (equal); Validation (equal); Visualization (equal); Writing – original draft (equal).

Florian Krüger: Resources (supporting); Software (supporting); Writing – review & editing (supporting). **Sang Ki Nam:** Project administration (equal); Resources (equal); Writing – review & editing (supporting).

Hoki Lee: Project administration (equal); Resources (equal); Writing – review & editing (supporting). **Suyoung Yoo:** Project administration (equal); Resources (equal); Writing – review & editing (supporting). **Jacob Eapen:** Formal analysis (equal); Methodology (equal); Validation (equal); Writing – review & editing (equal). **Mark J. Kushner:** Conceptualization

(equal); Investigation (equal); Methodology (equal); Supervision (equal); Writing – review & editing (lead). **Steven Shannon:** Conceptualization (equal); Funding acquisition (equal); Project administration (equal); Resources (equal); Supervision (equal); Writing – review & editing (equal).

DATA AVAILABILITY

The data that support the findings of this study are available from the corresponding author upon reasonable request.

REFERENCES

- ¹S. Subramanian *et al.*, “First monolithic integration of 3D complementary FET (CFET) on 300 mm wafers,” in *2020 IEEE Symposium on VLSI Technology*, Honolulu, Hawaii (IEEE, New York, 2020), pp. 1–2.
- ²H. Kim, S.-J. Ahn, Y. G. Shin, K. Lee, and E. Jung, “Evolution of NAND flash memory: From 2D to 3D as a storage market leader,” in *2017 IEEE International Memory Workshop (IMW)*, Monterey, California (IEEE, New York, 2017), pp. 1–4.
- ³C. G. Lee, K. J. Kanarik, and R. A. Gottscho, *J. Phys. D: Appl. Phys.* **47**, 273001 (2014).
- ⁴K. J. Kanarik, *J. Vac. Sci. Technol. A* **38**, 031004 (2020).
- ⁵H. Conrads and M. Schmidt, *Plasma Sources Sci. Technol.* **9**, 441 (2000).
- ⁶V. M. Donnelly and A. Kornblit, *J. Vac. Sci. Technol. A* **31**, 050825 (2013).
- ⁷Y. Zhang, M. J. Kushner, S. Sriraman, A. Marakhtanov, J. Holland, and A. Paterson, *J. Vac. Sci. Technol. A* **33**, 031302 (2015).
- ⁸S. Huang, C. Huard, S. Shim, S. K. Nam, I.-C. Song, S. Lu, and M. J. Kushner, *J. Vac. Sci. Technol. A* **37**, 031304 (2019).
- ⁹D. Ruixue, Y. Yintang, and H. Ru, *J. Semicond.* **30**, 016001 (2009).
- ¹⁰J.-H. Min, G.-R. Lee, J.-K. Lee, S. H. Moon, and C.-K. Kim, *J. Vac. Sci. Technol. B* **23**, 425 (2005).
- ¹¹W. Jin and H. H. Sawin, *J. Vac. Sci. Technol. A* **21**, 911 (2003).
- ¹²J.-K. Lee, I.-Y. Jang, S.-H. Lee, C.-K. Kim, and S. H. Moon, *J. Electrochem. Soc.* **157**, D142 (2010).
- ¹³K. Eriguchi, Y. Takao, and K. Ono, “A new aspect of plasma-induced physical damage in three-dimensional scaled structures—sidewall damage by stochastic straggling and sputtering,” in *2014 IEEE International Conference on IC Design & Technology* (IEEE, New York, 2014), pp. 1–5.
- ¹⁴A. Sarkar, J. Eapen, A. Raj, K. Murty, and T. D. Burchell, *J. Nucl. Mater.* **473**, 197 (2016).
- ¹⁵L. V. Zhitilei, Y. G. Yingling, T. E. Itina, T. A. Schoolcraft, and B. J. Garrison, *Int. J. Mass Spectrom.* **226**, 85 (2003).
- ¹⁶G. S. Oehrlein, R. J. Phaneuf, and D. B. Graves, *J. Vac. Sci. Technol. B* **29**, 010801 (2011).
- ¹⁷B. Helmer and D. Graves, *J. Vac. Sci. Technol. A* **16**, 3502 (1998).
- ¹⁸E. J. C. Tinacba, M. Isobe, K. Karahashi, and S. Hamaguchi, *Surf. Coat. Technol.* **380**, 125032 (2019).
- ¹⁹F. Gou, A. Kleyn, and M. Gleeson, *Int. Rev. Phys. Chem.* **27**, 229 (2008).
- ²⁰E. J. C. Tinacba, T. Ito, K. Karahashi, M. Isobe, and S. Hamaguchi, *J. Vac. Sci. Technol. B* **39**, 043203 (2021).
- ²¹J. Vegh *et al.*, *Appl. Phys. Lett.* **91**, 233113 (2007).
- ²²N. Nakazaki, Y. Takao, K. Eriguchi, and K. Ono, *Jpn. J. Appl. Phys.* **53**, 056201 (2014).
- ²³X. Hua, S. Engelmann, G. Oehrlein, P. Jiang, P. Lazzeri, E. Iacob, and M. Anderle, *J. Vac. Sci. Technol. B* **24**, 1850 (2006).
- ²⁴M. Armacost *et al.*, *IBM J. Res. Dev.* **43**, 39 (1999).
- ²⁵C. Cardinaud, M.-C. Peignon, and P.-Y. Tessier, *Appl. Surf. Sci.* **164**, 72 (2000).
- ²⁶C. Y. Ho, C. Lien, Y. Sakamoto, R. J. Yang, H. Fijita, C. Liu, Y. Lin, S. Pittikoun, and S. Aritome, *IEEE Electron Device Lett.* **29**, 1199 (2008).
- ²⁷H.-C. Scheer, N. Bogdanski, and M. Wissen, *Jpn. J. Appl. Phys.* **44**, 5609 (2005).
- ²⁸J. K. Kim, S. I. Cho, N. G. Kim, M. S. Jhon, K. S. Min, C. K. Kim, and G. Y. Yeom, *J. Vac. Sci. Technol. A* **31**, 021301 (2013).
- ²⁹J. Robertson, *Mater. Sci. Eng. R. Rep.* **37**, 129 (2002).
- ³⁰A. Nakano, R. K. Kalia, and P. Vashishta, *Phys. Rev. Lett.* **75**, 3138 (1995).
- ³¹A. P. Thompson *et al.*, *Comput. Phys. Commun.* **271**, 108171 (2021).
- ³²S. Munetoh, T. Motooka, K. Moriguchi, and A. Shintani, *Comput. Mater. Sci.* **39**, 334 (2007).
- ³³D. J. Evans and B. L. Holian, *J. Chem. Phys.* **83**, 4069 (1985).
- ³⁴S. Nose, *J. Phys.: Condens. Matter* **2**, SA115 (1990).
- ³⁵G. J. Martyna, D. J. Tobias, and M. L. Klein, *J. Chem. Phys.* **101**, 4177 (1994).
- ³⁶J. Tersoff, *Phys. Rev. B* **37**, 6991 (1988).
- ³⁷S. Wang and K. Komvopoulos, *Sci. Rep.* **10**, 8089 (2020).
- ³⁸P. Erhart and K. Albe, *Phys. Rev. B* **71**, 035211 (2005).
- ³⁹C. D. Wick, M. G. Martin, and J. I. Siepmann, *J. Phys. Chem. B* **104**, 8008 (2000).
- ⁴⁰A. Srivastava, “A molecular dynamics based study of bulk and finite polystyrene-carbon dioxide binary systems,” Ph.D. thesis (The Ohio State University, 2010).
- ⁴¹V. Harmandaris, N. Adhikari, N. F. van der Vegt, and K. Kremer, *Macromolecules* **39**, 6708 (2006).
- ⁴²J. Han and R. H. Boyd, *Polymer* **37**, 1797 (1996).
- ⁴³M. Kim, J. Moon, J. Choi, S. Park, B. Lee, and M. Cho, *Macromolecules* **51**, 6922 (2018).
- ⁴⁴B. P. Haley, N. Wilson, C. Li, A. Arguelles, E. Jaramillo, and A. Strachan, “Polymer Modeler,” *nanoHUB* (2022).
- ⁴⁵J. F. Ziegler and J. P. Biersack, “The stopping and range of ions in matter,” in *Treatise on Heavy-Ion Science*, Austin, Texas (Springer, Boston, Massachusetts, 1985), pp. 93–129.
- ⁴⁶K. K. Kammara, R. Kumar, and F. S. Donbosco, *Comput. Particle Mech.* **3**, 3 (2016).
- ⁴⁷A. A. Sycheva, E. N. Voronina, T. V. Rakhimova, and A. T. Rakhimov, *J. Vac. Sci. Technol. A* **36**, 061303 (2018).
- ⁴⁸A.-P. Prskalo, S. Schmauder, C. Ziebert, J. Ye, and S. Ulrich, *Surf. Coat. Technol.* **204**, 2081 (2010).
- ⁴⁹D. B. Graves and P. Brault, *J. Phys. D: Appl. Phys.* **42**, 194011 (2009).
- ⁵⁰P. A. Johnson, A. C. Wright, and R. N. Sinclair, *J. Non-Cryst. Solids* **58**, 109 (1983).
- ⁵¹B. Bhattacharai and D. Drabold, *Carbon* **115**, 532 (2017).
- ⁵²D. McCulloch, D. McKenzie, and C. Goringe, *Phys. Rev. B* **61**, 2349 (2000).
- ⁵³B. O’Malley, I. Snook, and D. McCulloch, *Phys. Rev. B* **57**, 14148 (1998).
- ⁵⁴G. Inc., see <http://www.goodfellow.com/E/Polystyrene.html> for “Polystyrene material information” (2021), accessed: 2021-09-12.
- ⁵⁵C. F. Abrams and D. B. Graves, *J. Vac. Sci. Technol. A* **16**, 3006 (1998).
- ⁵⁶A. Stukowski, *Modell. Simul. Mater. Sci. Eng.* **18**, 015012 (2009).
- ⁵⁷J. D. Hunter, *Comput. Sci. Eng.* **9**, 90 (2007).
- ⁵⁸M. Mitchell, B. Muffakhidinov, T. Winchen, A. Wilms, B. van Schaik, badshah400, Mo-Gul, T. G. Badger, Z. Jędrzejewski-Szmk, kensington, and kylesower: markummitchell/engauge-digitizer: Nonrelease (2020).
- ⁵⁹X. Mei, W. Mohamed, and J. Eapen, *Philos. Mag.* **98**, 2701 (2018).